Background scalar-level anisotropy caused by low-wave-number truncation in turbulent flows

L. Fang*
LMP, Ecole Centrale de Pékin, Beihang University, Beijing 100191, China
and Co-Innovation Center for Advanced Aero-Engine, Beihang University, Beijing 100191, China
(Received 18 October 2016; published 2 March 2017)

We rigorously show that the truncation at low wave numbers always leads to background scalar-level anisotropy at large scales. Neither the resolution nor the spectral low-pass filter is dominant for this anisotropy, while the shape of the energy spectrum at low wave numbers is an important influence factor. Quantitative results are shown to provide references to the statistics in future postprocessing studies. Also, a simplified analytical model is introduced to explain the single-mode effects for this anisotropy.

DOI: 10.1103/PhysRevE.95.033102

I. INTRODUCTION

Homogeneity and isotropy are two basic assumptions in many fundamental turbulence studies. In order to numerically generate homogeneous isotropic turbulence, the present method is to present the continuous physical field via a number of discrete points and to involve periodic conditions on the three dimensions [1–6]. The equivalent description of this discretization in Fourier spectral space is using a number of modes to represent the spectral information. As an ideal numerical case in turbulence, the Fourier-based discretized fields are expected to satisfy the spirit of homogeneity and isotropy, however, in recent years researchers have found several underlying defects of the Fourier description method. As an example, it was discussed that this discretization involves errors on *a posteriori* shell integrations [7]. Some other defects are related to the two truncations: (i) the high-wave-number truncation [8] yields a small-scale accumulation on the kinetic energy and, (ii) on another side, on the effects of the low-wave-number truncation, Brun and Pumir argued that these low-wave-number modes lead to intermittency [9]. Davidson qualitatively remarked that the low-wave-number truncation, which corresponds to the periodic conditions, will lead to unphysical large-scale anisotropy (see Chapter 7.2 of Ref. [10]). Recently, we have also shown that this anisotropy exists in direct numerical simulation (DNS) databases [11]. However, to our knowledge, there are no quantitative rigorous explanations for this anisotropy caused by low-wave-number truncation.

In order to clarify the present idea, here we classify the isotropy conditions in a homogeneous field to two levels:

(i) *The scalar-level isotropy condition.* In a homogeneous scalar field, a two-point statistical quantity should be the function of two-point distance $\vec{r}$ only. The scalar-level isotropy condition then requests that this statistical quantity is simply a function of r with $r = |\vec{r}|$. For example, under the isotropy condition the second-order correlation function of a statistically homogeneous scalar field $R_{\theta\theta}(\vec{r}) := \langle\theta(\vec{0})\theta(\vec{r})\rangle$ with θ scalar, $\langle\rangle$ ensemble average, and $\vec{r}$ two-point distance should be independent to the direction of $\vec{r}$, that is,

$$R_{\theta\theta}(\vec{r}) = R_{\theta\theta}(r). \tag{1}$$

This can also be defined by decomposing the scalar field into different modes with definite behaviors under rotations via the SO(3) symmetry group (cf. Refs. [12–16]) that $R_{\theta\theta}(\vec{r}) = \sum_{j,m} a_{j,m}(r)Y_{jm}(\hat{\vec{r}})$, in which the scalar-level isotropy corresponds to null coefficients for all nonzero modes. Similarly, the summation correlation function of velocity field $R_{ii}(\vec{r}) := \langle u_i(\vec{0})u_i(\vec{r})\rangle$ with $\vec{u}$ velocity, can also define a scalar-level isotropy condition

$$R_{ii}(\vec{r}) = R_{ii}(r). \tag{2}$$

(ii) *The tensor-level isotropy condition.* In a homogeneous vector or tensor field, a two-point statistical quantity is usually a tensor. The tensor-level isotropy condition then describes the relation among the tensor components. For example, the well-known relation between the second-order longitudinal and transverse structure functions reads [17]

$$D_{nn}(r) = D_{ll}(r) + \frac{r}{2}\frac{dD_{ll}(r)}{dr}, \tag{3}$$

where $D_{ll}(r) := \langle(u_1(r\vec{e}_1) - u_1(\vec{0}))^2\rangle$ is the longitudinal structure function, $D_{nn}(r) := \langle(u_1(r\vec{e}_2) - u_1(\vec{0}))^2\rangle$ is the transverse structure function, and the subscripts l and n represent the longitudinal and transverse components, respectively. From the SO(3) decomposition the tensor-level isotropy implies null coefficients for all nonzero modes of the tensor $\boldsymbol{D}$ with $\boldsymbol{D}(\vec{r}) = \sum_{q,jm} a_{q,jm}(r)\boldsymbol{B}_{jm}(\hat{\vec{r}})$. Note that conceptually the scalar-level isotropy condition is a precondition of the tensor-level isotropy condition.

These two levels were not well clarified in much of the literature. Usually, in the validation of DNS and large-eddy simulation (LES) cases (cf. Refs. [18,19]), researchers used Eq. (3) to estimate the "isotropy" of the generated turbulent field. However, as stated above, this "isotropy" belongs to the tensor level, which indeed depends on a scalar-level anisotropy condition that was not rigorously visited in literature.

References [10,11] qualitatively shows that periodic conditions lead to a background large-scale scalar-level anisotropy; however, underlying mechanism and quantitative description are still lacking. The present contribution aims at rigorously explaining the link between the large-scale scalar-level anisotropy and the low-wave-number truncation, and quantitatively showing the relation between this anisotropy and several possible factors, including the low-wave-number energy spectra.

*le.fang@zoho.com

II. THEORETICAL ANALYSIS

In the present contribution, the second-order summation correlation function $R_{ii}(\vec{r}) := \langle u_i(\vec{0})u_i(\vec{r})\rangle$ is chosen as an example for investigating the scalar-level anisotropy caused by low-wave-number truncation. We consider a discrete numerical case with period 2π and $2n+1$ independent grids [20] in each direction, thus all grid points constitute the following set in physical space:

$$\mathcal{R} = \{(r_1,r_2,r_3)|r_1,r_2,r_3 = \frac{2\pi j}{2n+1}, j = 0,1,\ldots,2n+1\}. \tag{4}$$

The discrete Fourier transform of these discrete points corresponds to the following set in spectral space:

$$\mathcal{K} = \{(k_1,k_2,k_3)|k_1,k_2,k_3 = -n,-n+1,\ldots, -1,0,1,\ldots,n-1,n\}. \tag{5}$$

From the properties of discrete Fourier transform and by using the homogeneous condition [21], we can write the following relations for the correlation function:

$$R_{ii}(\vec{r}) = \langle u_i(\vec{0})u_i(\vec{r})\rangle = \sum_{\vec{k}\in\mathcal{K}}\langle\hat{u}_i(\vec{k})\hat{u}_i(-\vec{k})\rangle e^{i\vec{k}\cdot\vec{r}} = \sum_{\vec{k}\in\mathcal{K}}\frac{E(k)}{2\pi k^2}e^{i\vec{k}\cdot\vec{r}}, \tag{6}$$

where

$$\hat{u}_i(\vec{k}) = \mathscr{F}(u_i(\vec{r})) = \frac{1}{8\pi^3}\sum_{\vec{r}\in\mathcal{R}}u_i(\vec{r})e^{-i\vec{k}\cdot\vec{r}}, \tag{7}$$

and $E(k)$ is the energy spectrum. Note that besides the second-order correlation functions, we can also write the third-order relations between physical and spectral quantities by using a similar procedure [21]; by contrast, the expressions for higher-order moments will not be obvious, which usually depends on an assumption of closure, such as the Gaussian assumptions [22–24]. In addition, although this expression is formally similar to the continuous results (cf. Ref. [21]), the discrete sets $\mathcal{K}$ and $\mathcal{R}$ are the spirits for describing the numerical truncations, as will be analyzed in the following parts. The minimum wave number is 1, implying that the period in each direction is always set as 2π in the present study.

III. RESULTS

As presented in the previous section, Eq. (6) describes the relation between the second-order correlation function and the energy spectrum via a discrete summation, which represents the effect of low-wave-number truncation. In this section, we will show that for a given energy spectrum, this discrete summation always leads to a scalar-level anisotropy for the second-order correlation function. In order to support this conclusion, the relation between this anisotropy and other factors will also be discussed in the following subsections, respectively.

A. Quantitative descriptions on background scalar-level anisotropy

As stated in the above parts, the background scalar-level anisotropy implies that the value of $R_{ii}(\vec{r})$ depends on not only the length but also the direction of $\vec{r}$. Extreme directions such as the axis direction and the face or cube diagonal directions can be chosen for comparison. Also, we can quantitatively define the standard variation in the spherical surface with radius r and denote

$$\mathcal{A}(r) = \frac{1}{R_{ii}(\vec{0})} \times\sqrt{\frac{2}{\pi}\int_{\theta=0}^{\pi/2}\int_{\phi=0}^{\pi/2}[R_{ii}(r,\theta,\phi)-\mu(r)]^2\sin\theta d\phi d\theta}, \tag{8}$$

with $\mu(r)$ the surface average of the scalar field under spherical coordinate $R_{ii}(r,\theta,\phi)$

$$\mu(r) = \frac{2}{\pi}\int_{\theta=0}^{\pi/2}\int_{\phi=0}^{\pi/2}R_{ii}(r,\theta,\phi)\sin\theta d\phi d\theta. \tag{9}$$

Note that here the spherical averages are performed in a 1/8 sphere because of symmetry. We remark that this is only a general description on the background scalar-level anisotropy. If we want to investigate more details about the anisotropy at different modes, an SO(3) decomposition should be necessary.

We perform a numerical case to show this background scalar-level anisotropy. We select $n = 35$ (corresponding to a 71^3 resolution) and the Kolmogorov 3/5 energy spectrum at all nonzero wave numbers,

$$E(k) = \begin{cases}0, & \text{if } k = 0,\\ k^{-5/3}, & \text{otherwise.}\end{cases} \tag{10}$$

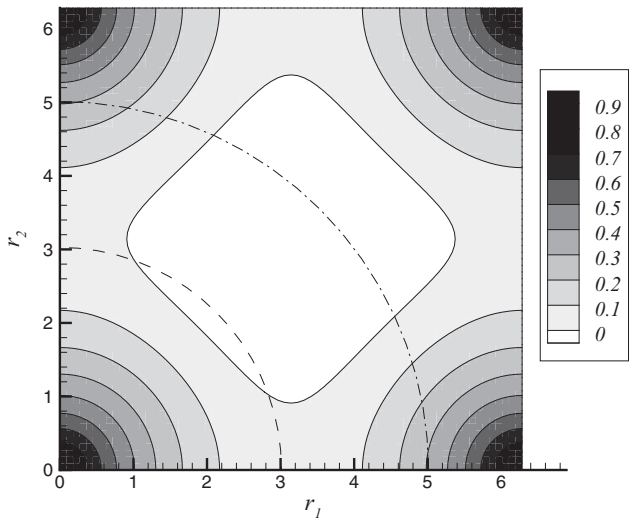

FIG. 1. $R_{ii}(\vec{r})$ with $r_3 = 0$ fixed. $R_{ii}(\vec{0})$ is used for normalization. The energy spectrum is Eq. (10). The half-grid number is $n = 35$. The dashed and the dash-dotted curves correspond to $r = 3$ and $r = 5$, respectively.

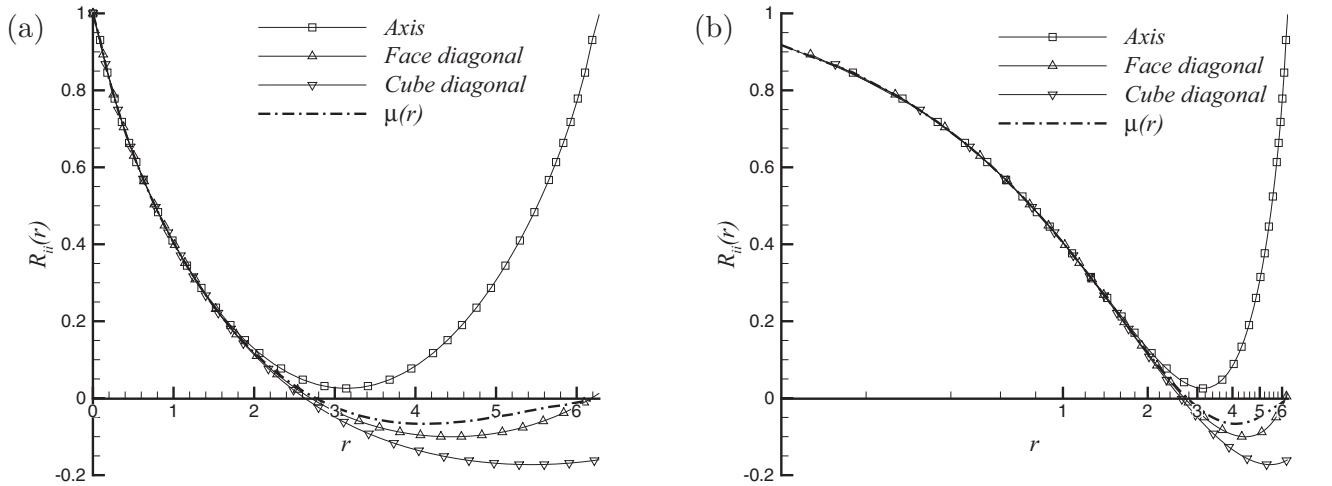

FIG. 2. $R_{ii}(\vec{r})$ with $\vec{r}$ in axis direction, face diagonal direction, and cube diagonal direction, respectively. $R_{ii}(\vec{0})$ is used for normalization. The energy spectrum is Eq. (10). The half-grid number is $n = 35$. The dash-dotted curve is the spherical average value of $R_{ii}(\vec{r})$ over the sphere with radius r. (a) Normal view; (b) log view.

Note that in the present case the discretization in spectral space implies that $E(k)$ is truncated at low wave numbers $k = 1$, and therefore Eq. (10) does not imply a discontinuous spectrum.

A two-dimensional contour at the r_1-r_2 plane where $r_3 = 0$ is presented in Fig. 1 to show the dependence of $R_{ii}(\vec{r})$ with the direction of $\vec{r}$. Clearly, at short scales where r is small (see the bottom-left corner in the figure), the constant value lines are approximately circular arcs, illustrating the fact of approximate small-scale isotropy. However, when r is large, this isotropy is broken. For instance, the value of $R_{ii}(\vec{r})$ is not a constant along the $r = 3$ arc (the dashed curve in the figure); this anisotropy is more obvious when r is larger, for instance, when $r = 5$ (see the dash-dotted curve in the figure). In addition, in the bottom-right, upper-left, and upper-right corners the values of $R_{ii}(\vec{r})$ are 1, corresponding to the periodicity at the low truncation wave number $k = 1$. In Fig. 2 we also compare the values of $R_{ii}(\vec{r})$ in typical directions to show this background scalar-level anisotropy. Similarly to the above discussion, the curves are almost the same at small r, but diverge at larger scales, implying that the background scalar-level anisotropy is a large-scale effect.

The quantitative description is shown in Fig. 3 by introducing the standard variation $\mathcal{A}(r)$ defined in Eq. (8). Consistent to the above discussions, the value of $\mathcal{A}(r)$ increases with the two-point distance r. The milestones of 1‰ and 1% variations correspond to $r = 1.44$ and 2.56, respectively. At larger scales, this variation can reach the order of 10%, which is in agreement of our previous study in DNS postprocessings [11].

B. Influence of resolution and spectral low-pass filters

The above calculations use $n = 35$ as the half-grid number. As presented in Fig. 4, changing the resolution does not lead to an obvious difference on the background scalar-level anisotropy. In each subfigure the curves are very close to each other, which means that the anisotropy effect is insensitive to resolution. Indeed, as the low-wave-number truncation is always fixed to $k = 1$, different resolutions only affect the high-wave-number descriptions, which correspond to small-scale details in physical space. Clearly, these small-scale details are not dominant for the background scalar-level anisotropy which occurs at large scales. This validation of resolution shows that the above discussion at $n = 35$ is robust to give resolution-independent results.

In practice we often use a low-pass filter in spectral space in numerical simulations, that is, using the set

$$\mathcal{K}' = \{\vec{k} \in \mathcal{K} \quad \text{and} \quad |\vec{k}| \leqslant n\} \tag{11}$$

to replace the set $\mathcal{K}$ in Eq. (6). Figure 5 clearly shows that there is no evident influence for the background scalar-level anisotropy by using the low-pass filter. The reason is the same as the effect of resolution, that all differences are in high wave numbers, which are not dominant for the background scalar-level anisotropy which occurs at large scales.

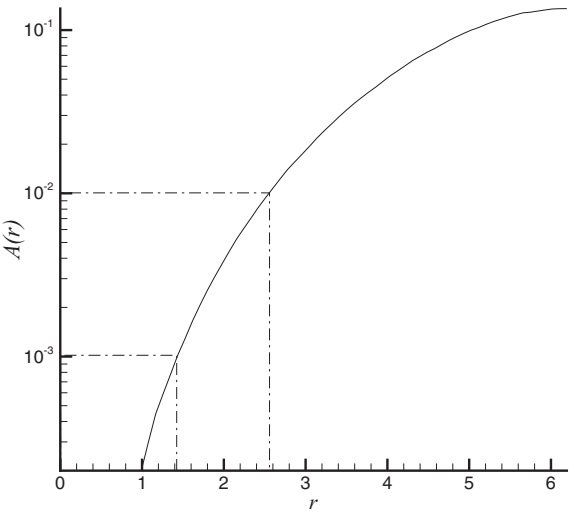

FIG. 3. The standard variation $\mathcal{A}(r)$. $R_{ii}(\vec{0})$ is used for normalization. The energy spectrum is Eq. (10). The half-grid number is $n = 35$. The dash-dotted lines show the positions of 1‰ and 1% variations, respectively.

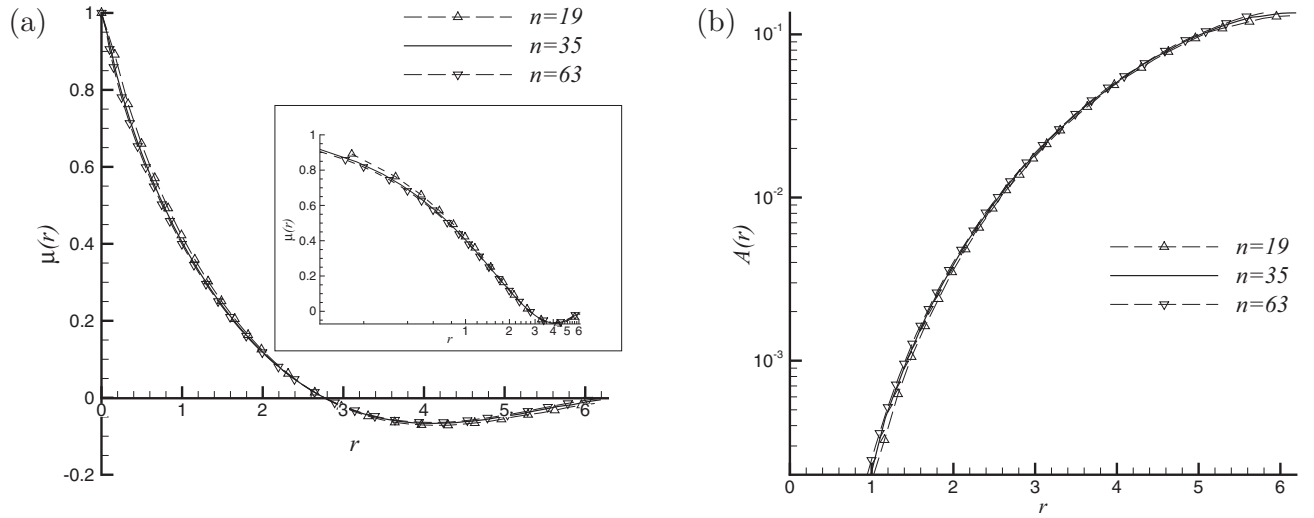

FIG. 4. Comparison of different resolutions. (a) Spherical average value $\mu(r)$ (subfigure: log view); (b) standard variation $\mathcal{A}(r)$. $R_{ii}(\vec{0})$ is used for normalization. The energy spectrum is Eq. (10).

C. Influence of energy spectrum

In the previous subsection, it was shown that the differences at high wave numbers are not dominant for the background scalar-level anisotropy. In order to investigate the influence of low wave numbers, we choose different energy spectra via the following formula:

$$E(k) = \begin{cases} k^2, & \text{if } k \leqslant k_p \\ k^{-5/3}, & \text{otherwise,} \end{cases} \tag{12}$$

with k_p the peak location which analogically corresponds to the energy-containing wave number. $k_p = 1$ is the case corresponding to Eq. (10). In this subsection we consider different energy spectra with $k_p = 1,2,3,4$, and 5, respectively, as presented in Fig. 6.

The spherical average values $\mu(r)$ are shown in Fig. 7(a). Clearly, with increasing k_p, the correlation function R_{ii} drops to zero faster. The underlying reason is that increasing k_p also damps the low-wave-number energies, which is dominant for the large-scale background anisotropy. Another analytical explanation will also be shown in Sec. IV. This property helps to reduce the large-scale background anisotropy, as shown in Fig. 7(b). For example, when $k_p = 3$, the milestones of 1‰ and 1% variations correspond to $r = 2.09$ and 5.20, respectively. Comparing to the $k_p = 1$ case in Sec. III A, this means that the isotropic range in the database is wider. Furthermore, we list in Table I the wave numbers in each case, respectively. In brief, larger value of k_p can efficiently reduce the background scalar-level anisotropy, because of the damping of low-wave-number energies.

We remark that in numerical simulations of forced turbulence, the forcing is usually added at energy-containing scales. From the present contribution we may conclude that if the forcing scale is close to the periodic size, then this forcing will definitively involve large-scale scalar-level anisotropy. In order to generate ideal isotropic turbulence, we therefore suggest

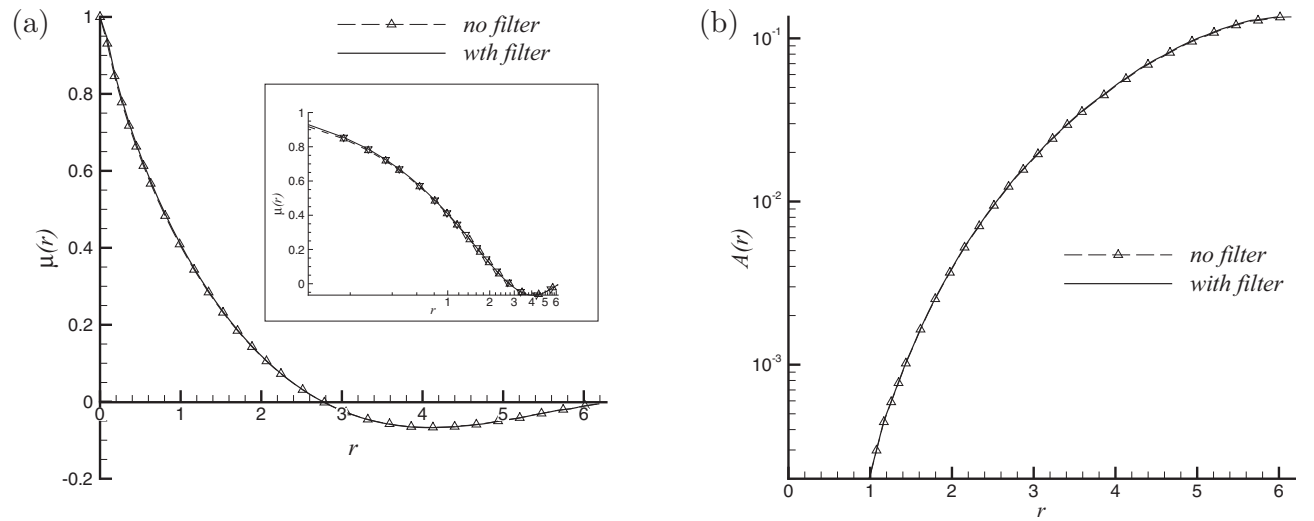

FIG. 5. Comparison of using isotropic filter in spectral space. (a) Spherical average value $\mu(r)$ (subfigure: log view); (b) standard variation $\mathcal{A}(r)$. $R_{ii}(\vec{0})$ is used for normalization. The half-grid number is $n = 35$. The energy spectrum is Eq. (10).

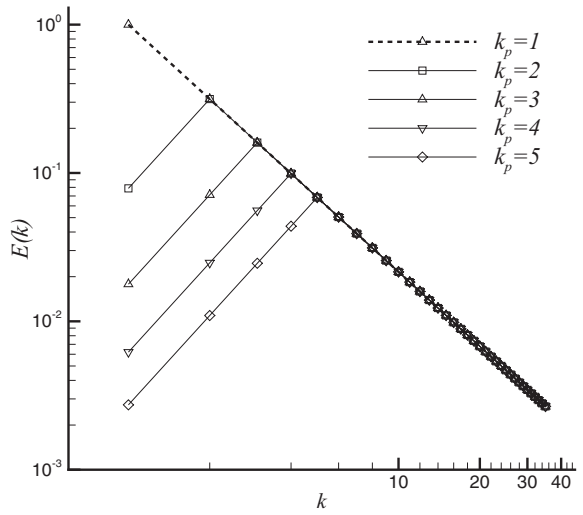

FIG. 6. Sketch of model spectra.

keeping a small forcing scale by comparing to the periodic size. In addition, by giving different forcing sizes, respectively, it might be interesting in future studies to investigate how the large-scale scalar-level anisotropy is transferred to small scales.

IV. A SIMPLIFIED ANALYTICAL MODEL

It is very difficult to give an analytical simplification for the correlation function R_{ii} using Eq. (6) under an arbitrary energy spectrum. However, here we introduce a simplified analytical model for separated single modes and obtain analytical relations to approximately explain the background scalar-level anisotropy. In this section we consider the correlation function of a scalar field $R_{\theta\theta}$ instead of R_{ii} for the modeling convenience, but the treatments for R_{ii} are exactly similar and the results do not change.

We assume that the energy spectrum is non-null at one wave number m, while it is null at other wave numbers. Specifically, the spectrum is isotropic and assumed to be discretized on only three axis directions in spectral space. This leads to a simple formula for the scalar field

$$\theta(x_1,x_2,x_3) = \cos(mx_1) + \cos(mx_2) + \cos(mx_3). \tag{13}$$

Due to the condition of spatial homogeneity, it is possible to translate the ensemble average operator to spatial average (similar ideas can be found in Refs. [25–27]). Therefore, when we select $\vec{r}$ with length r, in axis, face diagonal, and cube diagonal directions, respectively, the corresponding average value $R_{\theta\theta}$ (denoted as $R^{\mathrm{a}}_{\theta\theta}$, $R^{\mathrm{f}}_{\theta\theta}$, and $R^{\mathrm{c}}_{\theta\theta}$, respectively) can be analytically calculated as

$$\begin{aligned}
R^{\mathrm{a}}_{\theta\theta}(r) &= \frac{1}{64\pi^3 R_{\theta\theta}(\vec{0})}\int_{-2\pi}^{2\pi}\int_{-2\pi}^{2\pi}\int_{-2\pi}^{2\pi}\theta(x_1+r,x_2,x_3)\\
&\quad\times\theta(x_1,x_2,x_3)dx_1dx_2dx_3\\
&= \frac{2}{3}+\frac{1}{3}\cos(mr),\\
R^{\mathrm{f}}_{\theta\theta}(r) &= \frac{1}{64\pi^3 R_{\theta\theta}(\vec{0})}\int_{-2\pi}^{2\pi}\int_{-2\pi}^{2\pi}\int_{-2\pi}^{2\pi}\theta\left(x_1+\frac{\sqrt{2}}{2}r,x_2\right.\\
&\quad\left.+\frac{\sqrt{2}}{2}r,x_3\right)\theta(x_1,x_2,x_3)dx_1dx_2dx_3\\
&= \frac{1}{3}+\frac{2}{3}\cos\left(\frac{\sqrt{2}}{2}mr\right),\\
R^{\mathrm{c}}_{\theta\theta}(r) &= \frac{1}{64\pi^3 R_{\theta\theta}(\vec{0})}\int_{-2\pi}^{2\pi}\int_{-2\pi}^{2\pi}\int_{-2\pi}^{2\pi}\theta\left(x_1+\frac{\sqrt{3}}{3}r,x_2\right.\\
&\quad\left.+\frac{\sqrt{3}}{3}r,x_3+\frac{\sqrt{3}}{3}r\right)\theta(x_1,x_2,x_3)dx_1dx_2dx_3\\
&= \cos\left(\frac{\sqrt{3}}{3}mr\right),
\end{aligned} \tag{14}$$

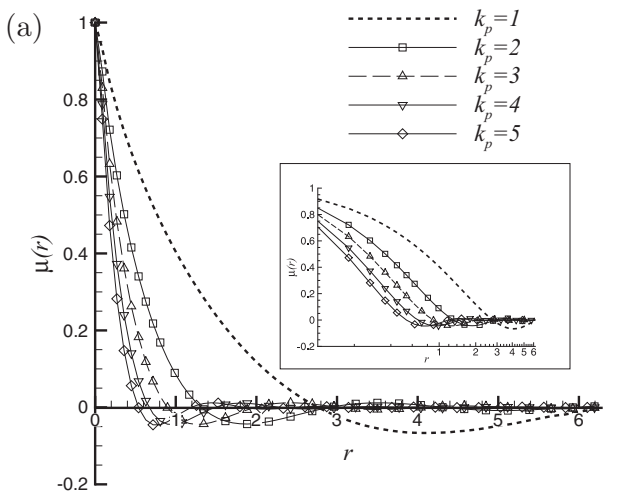

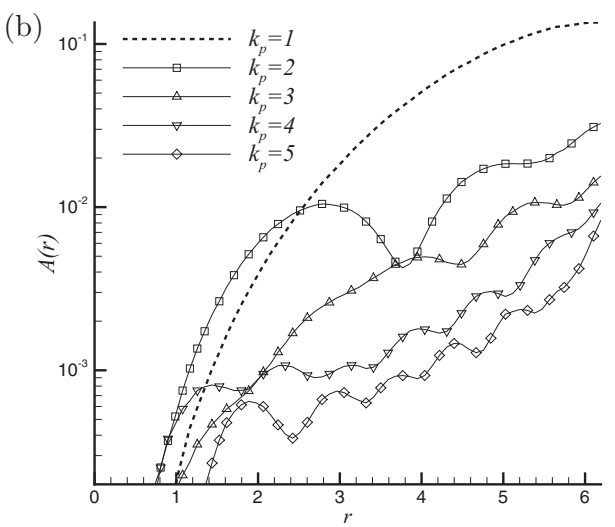

FIG. 7. Comparison of using different energy spectra. (a) Spherical average value $\mu(r)$ (subfigure: log view); (b) standard variation $\mathcal{A}(r)$. $R_{ii}(\vec{0})$ is used for normalization. The half-grid number is $n = 35$.

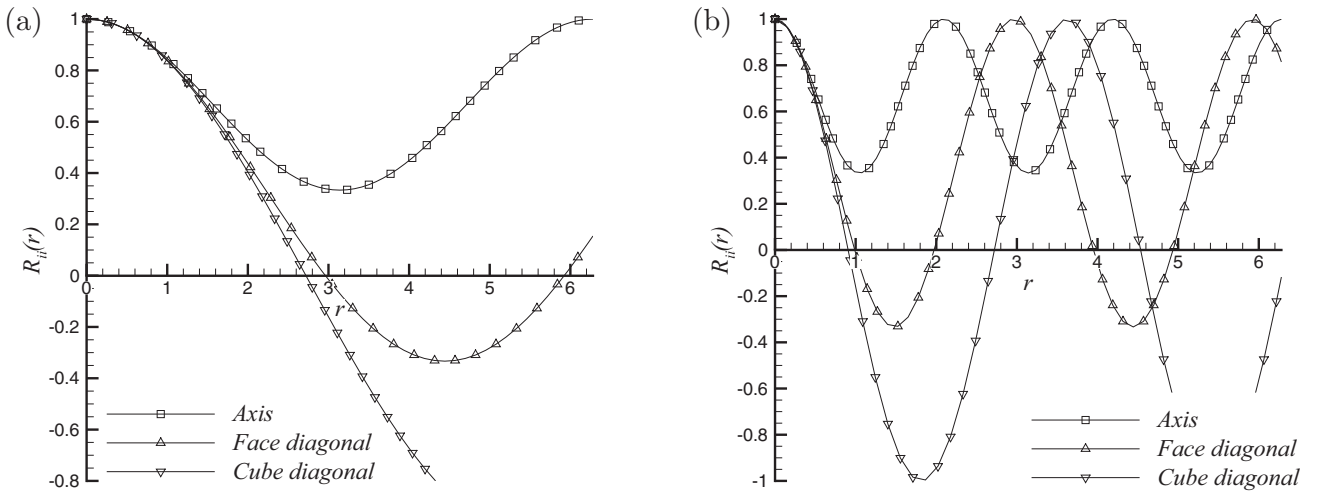

FIG. 8. $R_{ii}(\vec{r})$ with $\vec{r}$ in axis direction, face diagonal direction, and cube diagonal direction, respectively. $R_{ii}(\vec{0})$ is used for normalization. The simplified analytical model is used. (a) $m = 1$; (b) $m = 3$.

where

$$R_{\theta\theta}(\vec{0}) = \frac{1}{64\pi^3}\int_{-2\pi}^{2\pi}\int_{-2\pi}^{2\pi}\int_{-2\pi}^{2\pi}\theta(x_1,x_2,x_3)^2 dx_1 dx_2 dx_3 = \frac{3(4m^2\pi^2 + m\pi\sin(4m\pi) - 2\cos(4m\pi) + 2)}{8m^2\pi^2} \tag{15}$$

is employed for normalization.

This model can be then applied for explaining the background scalar-level anisotropy described in previous sections. Figure 8 presents the values of $R_{\theta\theta}(\vec{r})$ on these three typical directions by employing Eq. (14), with fixed modes $m = 1$ and $m = 3$, respectively. It is observed that the curves are almost the same at small r but diverge at larger scales, which agrees with the previous results (cf. Fig. 2). Also, higher wave numbers lead to faster reduction for $R_{\theta\theta}$ at small scales, which agrees with the conclusion of Sec. III C. We remark that this analytical model is only a quantitative theoretical explanation for the single-wave-number situation, which differs with real cases in which there are many nonlinear interactions among the wave numbers. As an example, when we consider the subharmonic functions in a turbulence field with specified energy relations [28], analytical models might also be derived. This will be an interesting investigation in the future. However, the objective of this analytical model is to introduce a preliminary theoretical framework, which is expected be improved in the future to take account of more complicated situations.

V. CONCLUSIONS

In the present study we rigorously show, by introducing the discrete Fourier transform, that the truncation at low wave numbers always yields large-scale anisotropy. This effect of anisotropy is compared with other effects and is considered as a background scalar-level anisotropy. It is shown that neither the resolution nor the spectral low-pass filter is dominant for this anisotropy; by contrast, the shape of energy spectrum at low wave numbers is quite important. Increasing the peak wave number leads to smaller anisotropy variation.

We then summarize the following conclusions and suggestions:

(a) The background scalar-level anisotropy is a congenital defect of numerical simulations for generating isotropic turbulent flows, which differs from traditional studies of the tensor-level anisotropy effect. This means that with low-wave-number truncation, there will always be anisotropic structures at large scales, which cannot be completely avoided. This may affect the accuracy of statistics in the numerical data of DNS and LES, since usually we wish they to be "isotropic". In particular, the quantitative results in the present contribution, for instance in Table I, could be a reference for guiding the statistics in future postprocessing studies.

(b) Although the background scalar-level anisotropy cannot be eliminated, it can be efficiently reduced by simply damping the low-wave-number energies or increasing the energy-containing wave number (analogically corresponding to k_p of the present study). In practice, this means that the energy-containing scale should be much smaller than the period. This is indeed consistent with many existing high-quality DNS databases [2,4,18,29]. By contrast, neither the resolution nor the spectral low-pass filter is dominant for the background scalar-level anisotropy.

(c) The present conclusions are consistent to the structure functions D_{ii} due to the relation $D_{ii} = 2 - 2R_{ii}$ [using $R_{ii}(\vec{0})$ for normalization]. Furthermore, the similar method can be extended to higher-order structure functions by using the Gaussian assumptions. Indeed, it can be found that for higher-order structure functions, the background scalar-level

TABLE I. Wave-number positions of 1‰ and 1% variations using different energy spectra. The half-grid number is $n = 35$.

	$k_p = 1$	$k_p = 2$	$k_p = 3$	$k_p = 4$	$k_p = 5$
1‰ variation	1.44	1.16	2.09	2.14	4.08
1% variation	2.56	2.68	5.20	6.15	$>2\pi$

anisotropy is more obvious, since it is affected by even larger deviations depending on the "dynamical" evolution of the velocity field. Indeed, the presence of a periodic box is trivially breaking isotropy of any field at large scales, and it will be efficient to use the SO(3) decomposition in the future to have a systematic control of isotropic and anisotropic fluctuations for any scalar or tensor correlation function.

ACKNOWLEDGMENTS

We are grateful to Wouter Bos and Zecong Qin for the discussions and to the two anonymous referees for the many constructive suggestions. This work is supported by the National Science Foundation in China (Grants No. 11572025 and No. 51420105008).

[1] R. S. Rogallo, Numerical experiments in homogeneous turbulence, NASA TM 81315, 1981.
[2] T. Watanabe and T. Gotoh, Statistics of a passive scalar in homogeneous turbulence, New J. Phys. **6**, 40 (2004).
[3] T. Ishihara, Y. Kaneda, M. Yokokawa, K. Itakura, and A. Uno, Small-scale statistics in high-resolution direct numerical simulation of turbulence: Reynolds number dependence of one-point velocity gradient statistics, J. Fluid Mech. **592**, 335 (2007).
[4] Y. Li, E. Perlman, M. Wan, Y. Yang, C. Meneveau, R. Burns, S. Chen, A. Szalay, and G. Eyink, A public turbulence database cluster and applications to study lagrangian evolution of velocity increments in turbulence, J. Turb. **9**, N31 (2008).
[5] T. Gotoh, T. Watanabe, and Y. Suzuki, Universality and anisotropy in passive scalar fluctuations in turbulence with uniform mean gradient, J. Turb. **12**, N48 (2011).
[6] L. Fang, W. J. T. Bos, L. Shao, and J.-P. Bertoglio, Time-reversibility of Navier-Stokes turbulence and its implication for subgrid scale models, J. Turb. **13**, N3 (2012).
[7] R. Stepanov and F. Plunian, Systematic bias in the calculation of spectral density from a three-dimensional spatial grid, Phys. Rev. E **90**, 053309 (2014).
[8] W. J. T. Bos and J. P. Bertoglio, Dynamics of spectrally truncated inviscid turbulence, Phys. Fluids **18**, 071701 (2006).
[9] C. Brun and A. Pumir, Statistics of fourier modes in a turbulent flow, Phys. Rev. E **63**, 056313 (2001).
[10] P. A. Davidson, *Turbulence: An Introduction for Scientists and Engineers* (Oxford University Press, Oxford, 2004).
[11] Z. C. Qin, L. Fang, and J. Fang, How isotropic are turbulent flows generated by using periodic conditions in a cube? Phys. Lett. A **380**, 1310 (2016).
[12] I. Arad, V. S. L'vov, and I. Procaccia, Correlation functions in isotropic and anisotropic turbulence: The role of the symmetry group, Phys. Rev. E **59**, 6753 (1999).
[13] A. L. Fairhall, O. Gat, V. L'vov, and I. Procaccia, Anomalous scaling in a model of passive scalar advection: Exact results, Phys. Rev. E **53**, 3518 (1996).
[14] V. L'vov and I. Procaccia, The universal scaling exponents of anisotropy in turbulence and their measurement, Phys. Fluids **8**, 2565 (1996).
[15] L. Biferale and I. Procaccia, Anisotropy in turbulent flows and in turbulent transport, Phys. Rep. **414**, 43 (2005).
[16] C. M. Casciola, P. Gualtieri, B. Jacob, and R. Piva, The residual anisotropy at small scales in high shear turbulence, Phys. Fluids **19**, 101704 (2007).
[17] J. O. Hinze, *Turbulence*, 2nd ed. (McGraw-Hill, New York, 1975).
[18] T. Gotoh, D. Fukayama, and T. Nakano, Velocity field statistics in homogeneous steady turbulence obtained using a high-resolution direct numerical simulation, Phys. Fluids **14**, 1065 (2002).
[19] G. X. Cui, H. B. Zhou, Z. S. Zhang, and L. Shao, A new dynamic subgrid eddy viscosity model with application to turbulent channel flow, Phys. Fluids **16**, 2835 (2004).
[20] Assuming an odd number of grids will simply lead to a symmetric description in spectral space.
[21] W. J. T. Bos, L. Chevillard, J. Scott, and R. Rubinstein, Reynolds number effects on the velocity increment skewness in isotropic turbulence, Phys. Fluids **24**, 015108 (2012).
[22] M. Lesieur, *Turbulence in Fluids* (Kluwer Academic, Dordrecht, 1997).
[23] S. A. Orszag, Lectures on the statistical theory of turbulence, in *Fluid Dynamics, Les Houches Summer School of Theoretical Physics*, edited by R. Balian and J.-L. Peube (Gordon and Breach, New York, 1974).
[24] L. Fang, Y. J. Zhang, J. Fang, and Y. Zhu, Relation of the fourth-order statistical invariants of velocity gradient tensor in isotropic turbulence, Phys. Rev. E **94**, 023114 (2016).
[25] L. Fang, W. J. T. Bos, and G. D. Jin, Short-time evolution of Lagrangian velocity gradient correlations in isotropic turbulence, Phys. Fluids **27**, 125102 (2015).
[26] L. Fang, X. Y. Sun, and Y. W. Liu, A criterion of orthogonality on the assumption and restrictions in subgrid-scale modeling of turbulence, Phys. Lett. A **380**, 3988 (2016).
[27] L. Fang and M. W. Ge, Mathematical constraints in multiscale subgrid-scale modeling of nonlinear systems, Chin. Phys. Lett. **34**, 030501 (2017).
[28] F. Plunian and K. H. Rädler, Subharmonic dynamo action in the Roberts flow, Geophys. Astrophys. Fluid Dyn. **96**, 115 (2002).
[29] T. Gotoh and D. Fukayama, Pressure Spectrum in Homogeneous Turbulence, Phys. Rev. Lett. **86**, 3775 (2001).